The Journal of Chemical Physics

Morphology and reactivity of size-selected titanium oxide nanoclusters on Au(111)

Cite as: J. Chem. Phys. **152**, 054714 (2020); https://doi.org/10.1063/1.5134453
Submitted: 30 October 2019 . Accepted: 14 January 2020 . Published Online: 04 February 2020

Kenneth R. Goodman, Jason Wang, Yilin Ma, Xiao Tong, Dario J. Stacchiola, and Michael G. White

COLLECTIONS

Paper published as part of the special topic on Oxide Chemistry and Catalysis
Note: This article is part of the JCP Special Topic on Oxide Chemistry and Catalysis.

This paper was selected as Featured

The Journal of Chemical Physics ARTICLE scitation.org/journal/jcp

Morphology and reactivity of size-selected titanium oxide nanoclusters on Au(111)

Cite as: J. Chem. Phys. 152, 054714 (2020); doi: 10.1063/1.5134453
Submitted: 30 October 2019 • Accepted: 14 January 2020 •
Published Online: 4 February 2020

Kenneth R. Goodman,[1] Jason Wang,[1] Yilin Ma,[1] Xiao Tong,[2] Dario J. Stacchiola,[2] and Michael G. White[1,3,a)]

AFFILIATIONS

[1] Department of Chemistry, Stony Brook University, Stony Brook, New York 11794, USA
[2] Center for Functional Nanomaterials, Brookhaven National Laboratory, Upton, New York 11973, USA
[3] Chemistry Division, Brookhaven National Laboratory, Upton, New York 11973, USA

Note: This article is part of the JCP Special Topic on Oxide Chemistry and Catalysis.
[a)] **Author to whom correspondence should be addressed:** mgwhite@bnl.gov and michael.g.white@stonybrook.edu

ABSTRACT

The morphology and reactivity of mass-selected titania clusters, Ti_3O_6 and Ti_3O_5, deposited onto Au(111) were studied by scanning tunneling microscopy and temperature programmed desorption. Despite differing by only one oxygen atom, the stoichiometric Ti_3O_6 and the sub-stoichiometric ("reduced") Ti_3O_5 clusters exhibit very different structures and preferred binding sites. The Ti_3O_6 clusters bind at step edges and form small assemblies (2–4 clusters) on Au terraces, while the "reduced" Ti_3O_5 clusters form much larger fractal-like assemblies that can extend across step boundaries. Annealing the $Ti_3O_{5,6}$/Au(111) systems to higher temperatures causes changes in the size-distributions of cluster assemblies, but does not lead to the formation of TiO_x nanoislands for temperatures ≤700 K. Reactivity studies show that the reduced Ti_3O_5 cluster has higher activity than Ti_3O_6 for 2-propanol dehydration, although both clusters exhibit substantial activity for dehydrogenation to acetone. Calculations using DFT+U suggest that the differences in aggregate morphology and reactivity are associated with the number of undercoordinated Ti_{3c} sites in the supported clusters.

I. INTRODUCTION

Interfaces between metals and metal oxides play important roles in heterogeneous catalysis where the oxide can act as an unreactive support for dispersed metals (spectator), as an active participant in the catalytic reaction (multifunctional catalyst), or as a chemical modifier to oxide supported metals (promoter). Reducible oxides (e.g., titania and ceria) typically exhibit strong electronic interactions with metals that can stabilize oxygen anion vacancies in the oxide, alter the charge state or morphology of the metal nanoparticles (NPs), or create unique metal–oxide interface sites.[1–4] For Cu–ceria catalysts, both conventional (Cu nanoparticles deposited on CeO_2) and "inverse" (CeO_x nanoparticles on Cu) catalysts exhibit very high activity for the water–gas-shift reaction (WGSR).[5–7] The high activity is associated with the formation of oxygen vacancies in the oxide, which are stabilized by Cu → oxide electron transfer.[8,9] Similarly, both conventional Au/TiO_2 and "inverse" TiO_x/Au(111)[10] catalysts are highly active for low temperature CO oxidation, but, here, the activity is associated with unique Au–Ti^{4+} perimeter sites that bind and activate O_2.[11–17] Recent studies have also shown that titania supported Au nanoparticles can be encapsulated by TiO_x overlayers during high temperature reduction,[18] which is a manifestation of the so-called strong metal support interaction (SMSI).[19,20] Oxide encapsulation following reduction is common for many systems, e.g., Pt/CeO_x, Pt/TiO_2, Rh/TiO_2, and Cu/ZnO, and in some cases, this inverse oxide–metal configuration may be present under industrially relevant reaction conditions.[10,21–24]

As noted above, "inverse" model catalysts composed of metal oxide nanoparticles (or larger islands) deposited onto metal surfaces are often used to investigate the properties of metal–metal oxide interfaces.[25–28] Nanoparticles or islands of oxides supported on a metal surface can have unique structures, composition, and chemical properties that are not present in the bulk oxide due to strong

electronic interactions with the metal support and 2D confinement on the surface.[25,26] These can influence adsorbate interactions and reactivity by presenting unique cation coordination centers in the oxide and oxide–metal interface sites.[28] For the CeO_x/Cu and TiO_x/Au systems cited above, the reported catalytic activity is actually better than the conventional oxide supported metal catalyst.[6,10] Inverse catalysts also have the practical advantage of a conducting metal substrate, which allows the use of electron spectroscopic and structural probes [XPS/UPS, ISS, LEED, and scanning tunneling microscopy (STM)] for surface characterization without charging. We have recently examined the correlations of electron transfer measured by laser photoemission with reactivity for water dissociation for a number of metal oxide nanoclusters M_xO_y (M = Ti, Nb, Mo, and W) deposited on Cu(111) as model inverse catalysts for the WGSR.[29–31] In those studies, mass-selected cluster deposition was used to prepare M_xO_y/Cu(111) surfaces, which allows independent control of cluster size, coverage, and stoichiometry, i.e., metal-to-oxygen ratio. The latter made it possible to investigate the role of cation coordination and the role of O-atom vacancies on the electron transfer with the Cu support and water dissociation reactivity. For $Nb_3O_{5,7}$ clusters on Cu(111), temperature cycling of the surface during repeated water temperature programmed desorption (TPD) runs did not result in the loss of reactivity, indicating that the clusters were not deactivated.[30] By comparison, oxide-supported nanoparticles of Cu or Au often sinter into larger 3D metal nanoparticles under reaction conditions, which reduces their activity by the loss of active sites.[32–37]

In this work, we present the results of an STM study to investigate the binding sites and thermal stability of mass-selected Ti_xO_y (x/y = 3/5, 3/6) deposited on Au(111). This inverse system was chosen as previous studies of the TiOx/Au(111) surface prepared by vapor deposition exhibited activity for both low temperature CO oxidation and partial oxidation of alcohols.[10,38,39] Moreover, the Au–TiO_x interface was thought to play an important role in the reactivity.[39] The titania structures in these previous reactivity studies were mostly crystalline, nanoislands of TiO_2 in the 5–10 nm size range. Only Ti deposited onto multilayers of H_2O or NO_2 [reactive layer assisted deposition (RLAD)] resulted in small nanoparticles of TiO_2 (~1 nm) similar in size to those deposited here; annealing these small nanoparticles to high temperature (700–900 K) resulted in the growth of larger crystallites (~5 nm).[40,41] Independent control of stoichiometry and particle growth is not possible using such vapor deposition methods, but here we are able to show that clusters that differ by only one oxygen atom, i.e., Ti_3O_5 and Ti_3O_6, exhibit very different surface morphologies and preferred binding sites. Specifically, the Ti_3O_6 clusters preferentially bind at step edges and form small assemblies of 2–4 clusters on Au terraces, while the "reduced" Ti_3O_5 clusters form much larger fractal-like assemblies that can extend across step boundaries. Annealing the $Ti_3O_{5,6}$/Au(111) surfaces to higher temperatures (≤700 K) causes changes in the size-distributions of cluster assemblies, but does not lead to the formation of larger 2D nanoislands. The two $Ti_3O_{5,6}$/Au(111) surfaces also exhibit distinct reactivity, with the sub-stoichiometric Ti_3O_5 cluster showing significantly higher activity for the decomposition (dehydration and dehydrogenation) reactions of 2-propanol than the stoichiometric Ti_3O_6 cluster.

II. METHODS

A. Experiments

Experiments were carried out in two different instruments each equipped with cluster deposition sources connected to UHV sample chambers housing surface science instrumentation for substrate cleaning and surface characterization. In both instruments, the Ti_xO_y clusters were generated by a reactive sputtering source using a DC magnetron source (Oxford Applied Research, NC200U-B), in which a metal (Ti) target was sputtered with a gas mixture of roughly 2% O_2 in Ar and helium was used as an aggregation gas to promote cluster condensation. Typical running powers of the magnetron sources were ~175 W. After exiting the source, cluster ions were mass selected by a downstream quadrupole mass filter and separated from neutrals via a quadrupole bender prior to deposition onto the Au(111) surface at low kinetic energies (<0.3 eV/atom). Typical deposition ion currents for mass-selected $Ti_xO_y^+$ clusters were ~0.5 nA and a representative mass distribution is shown in Fig. 1. The surfaces for STM studies were prepared by depositing 2×10^{13} clusters in a ~5 mm diameter spot on the Au(111) surface.[29] To allow comparison between the surfaces with different clusters, STM images were recorded in regions of the surface where the cluster coverage was determined to be approximately the same, ~0.25 ML.

The Au(111) crystals were cleaned by alternating cycles of Ar ion sputtering (1 keV beam energy for 30 min) and annealing in UHV (~800 K for 30 min). Sample cleanliness prior to deposition was confirmed with AES and XPS.

For the STM measurements, the Au(111) substrate was mounted on a flag-style sample plate (stainless steel) that could be heated from the back by electron impact from a filament located on the sample receiver, which, in turn, was mounted to a 4-axis UHV manipulator. In this instrument, the sample could be moved between the cluster deposition chamber, the UHV characterization chamber, and the sample transfer chamber via a combination of linear manipulators and wobble sticks. Transport of the sample to the STM instrument was accomplished using a portable vacuum suitcase, which was actively pumped by a getter pump (SAES Getters, Capacitor Z-100) to maintain UHV conditions.

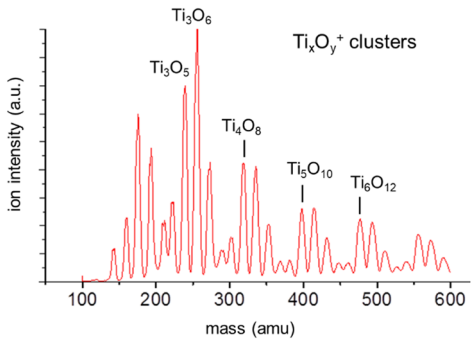

FIG. 1. Typical mass distribution of $Ti_xO_y^+$ clusters produced by reactive sputtering with a DC magnetron source.

Scanning tunneling microscopy (STM) images on Ti_3O_x/Au(111) surfaces were obtained in constant current mode using an Omicron VT-STM-XA650 located at the Center for Functional Nanomaterials at Brookhaven National Laboratory. All the images presented in this work were scanned at room temperature using a Pt/Ir tip with a positive sample bias (typically ~2.0 V and ~400 pA). To examine the effects of surface annealing, the samples were heated to temperatures between 400 K and 700 K for 3 min and then cooled back to room temperature before imaging. STM images were analyzed using WSxM software (version 5.0).[42]

Reactivity studies of the $Ti_3O_{5,6}$/Au(111) surfaces were carried out in a second instrument using temperature programmed desorption (TPD) measurements. A 2-propanol sample was degassed by several freeze–pump–thaw cycles prior to the experiments. Dosing of the samples was performed by leaking a small volume of 2-propanol vapor through a 50 μm (diam) aperture connected to a stainless-steel tube (6 mm diam) placed a few millimeters away from the sample surface held at 120 K. For the TPD measurements, the sample was placed in front of the entrance aperture of a quadrupole mass spectrometer (Hiden Analytical), which monitored multiple masses simultaneously. The heating rate for TPD measurements was 2 K/s. For these experiments, about 3×10^{13} clusters were deposited in a ~5 mm diameter spot; assuming a cluster diameter of 5 Å [based on density functional theory (DFT) calculated adsorption structures], this number of deposited ions corresponds to a coverage of ~0.3 ML.

The oxidation states of the Ti atoms in the deposited clusters were probed by the Ti 2p core level using XPS instruments located in the cluster deposition and STM instruments. In all cases, XPS spectra were obtained using unmonochromatized Al K_α radiation (1486.6 eV) and hemispherical electron energy analyzers. The Au $4f_{7/2}$ binding energy (83.8 eV) from the Au(111) substrate was used as the reference energy for all spectra. The XPS peak fitting was carried out using the XPSPeak software (version 4.1) with Shirley background contributions. The FWHMs were set to be equal for the spin–orbit doublet peaks.

B. Theoretical (DFT) calculations

Spin-polarized, density functional theory (DFT) calculations were performed using the Vienna *Ab Initio* Simulation Package (VASP)[43–45] to study the geometry and adsorption energy of titanium oxide clusters on the Au (111) surface. Generalized gradient approximations (GGAs) by Perdew *et al.*[46] were applied for the exchange-correlation functional. The projector-augmented wave (PAW) method[47] was used to describe the electron-ion interactions, where the cutoff energy of the plane-wave basis set was set to 400 eV. The O (2s, 2p), Ti(4s, 3d), and Au(5d, 6s) were treated as valence electrons. A Gaussian smearing of 0.05 eV was applied for faster convergence.

For transition metal oxides such as titania, the GGA method suffers from a significant underestimation of the bandgap, where the d-electrons of the transition oxide tend to over-delocalize. To improve the calculations, the GGA+U approach proposed by Dudarev *et al.* has been employed.[48] Calculations for single clusters on the Au(111) surface were performed with U values of 2.5 eV and 4.5 eV, which span the range typically used to describe Ti 3d levels.[29,31,49,50] The resulting optimized cluster structures on the Au(111) surface were essentially identical for both U values, and only the results for U = 2.5 eV are reported here.

A three-layer slab of Au (111) separated by more than 20 Å of vacuum was used for all systems to prevent interactions from neighboring cells. A (2 × 2) supercell was used for modeling a single cluster on the surface with the bottom layer of atoms fixed and top two layers relaxed. The Brillouin-zone integrations were performed by a gamma centered K-point grid of (3 × 3 × 1) in the Monkhorst–Pack scheme.[51] After geometry optimization of the Au(111) supercell, clusters with gas-phase structures obtained from previous studies[29,52–54] were placed on the Au surface with different initial orientations. This geometry optimization is reasonable given that we are depositing clusters from the gas-phase, but may not represent global minimum energy structures, especially if the latter involve atom re-arrangements via bond breaking.

Cluster adsorption energies, E_{ads}, were calculated using the expression

$$E_{ads} = E_{cluster/Au} - (E_{cluster} + E_{Au}), \quad (1)$$

where $E_{cluster/Au}$ is the energy of supported clusters on the Au(111) substrate, $E_{cluster}$ is the energy of the optimized gas-phase cluster, and E_{Au} is the energy of the bare Au(111) substrate.

III. RESULTS AND DISCUSSION

A. Oxidation state of Ti atoms

The Ti 2p core level spectra for the Ti_3O_5 and Ti_3O_6 clusters deposited on Au(111) are shown in Fig. 2. The spectrum for the sub-stoichiometric ("reduced") Ti_3O_5 cluster clearly shows a larger

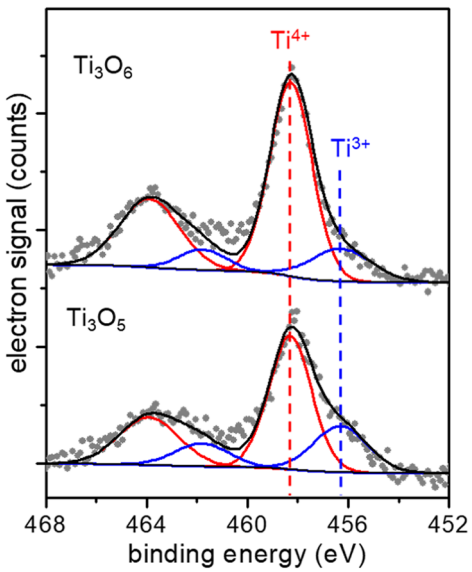

FIG. 2. Ti 2p core level spectra for Ti_3O_6 (top) and Ti_3O_5 (bottom) clusters supported on Au(111). Least-squares fits show contributions from Ti^{4+} (red) and Ti^{3+} (blue) oxidation states.

contribution from reduced Ti^{3+} cations (~30% of the total Ti signal), which are attributed to the presence of undercoordinated Ti cations associated with the oxygen "vacancy." Although the Ti^{4+} signal is larger for the stoichiometric Ti_3O_6 cluster, it still contains a significant fraction of Ti^{3+} (~19%). The differences in Ti^{3+}/Ti^{4+} ratios are discussed in more detail in Sec. III C in relation to the DFT calculated cluster structures on Au(111). The ratio of the oxygen 1s core level intensities for the Ti_3O_6 and Ti_3O_5 surfaces is 1.23 ± 0.08, which brackets the expected 6:5 oxygen atom ratio. The calibrated binding energies of the Ti^{4+} $2p_{3/2}$ peaks are within ±0.5 eV of those measured for other TiO_x islands on Au(111)[40,55] as well as the TiO_2(110) crystal surface itself.[56] The XPS data confirm that the as-deposited Ti_3O_5 and Ti_3O_6 clusters have distinct electronic properties, which, as described below, are ultimately responsible for the observed differences in cluster morphology and reactivity toward partial oxidation of 2-propanol on the Au(111) surface.

B. Surface morphology

1. Surface morphology at room temperature

The STM images presented in Fig. 3 for the as-deposited Ti_3O_6 and Ti_3O_5 clusters on Au(111) surfaces (~0.25 ML) show clear differences in surface morphology despite only differing by one O-atom. For both surfaces, the small particles appear to form assemblies that are randomly oriented on the terraces with no apparent registration to the underlying Au(111) structure. We identify the discrete particles with individual clusters. Tip effects were evident, especially at low and negative bias, where it was difficult to image the clusters as they appeared to be dragged across the surface by the tip. For the Ti_3O_6/Au(111) surface, the cluster assemblies have a mean size of ~4 clusters, but the clusters remain distinguishable as individual oval-shaped structures that touch along the long direction [see Fig. 3(c)]. The cluster assemblies are much larger on the Ti_3O_5/Au(111) surface with a mean size of ~30 clusters. More interestingly, the Ti_3O_5 clusters form fractal-like structures with extended dendrites composed of clusters in close contact [see Fig. 3(d)]. The calculated fractal dimension for multiple cluster assemblies, 1.70 ± 0.02, is very close to the theoretical value of 1.7 for 2D simulations of diffusion limited aggregation.[57–59] The measured area distributions for both cluster surfaces and the fractal dimension calculations for Ti_3O_5 cluster assemblies are given in the supplementary material (Figs. S1–S3). The formation of cluster assemblies on both surfaces suggests that cluster diffusion barriers on the terraces can be overcome at room temperature and that inter-cluster interactions are strong enough to cause cluster aggregation, but are apparently too weak to result in the loss of chemical identity through the formation of TiO_x islands.

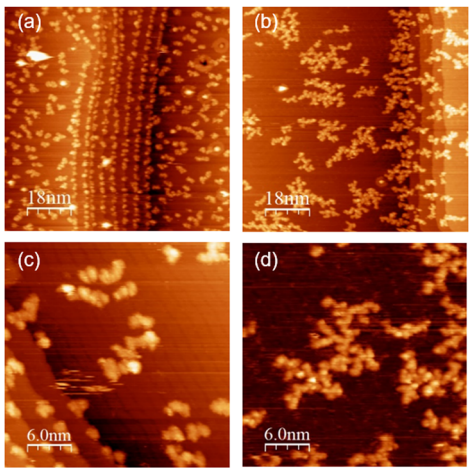

FIG. 3. STM images of as-deposited clusters on Au(111) taken at room temperature: (a) Ti_3O_6 clusters (0.26 ML, U = 2.0 V, I = 300 pA, image size 90 nm × 90 nm); (b) Ti_3O_5 clusters (0.24 ML, U = 2.0 V, I = 200 pA, image size 90 nm × 90 nm); (c) Ti_3O_6 clusters (U = 2.0 V, I = 300 pA, image size 30 nm × 30 nm); (d) Ti_3O_5 clusters (U = 1.7 V, I = 500 pA, image size 30 nm × 30 nm).

The clusters also show markedly different behavior for binding at Au(111) step edges (see Fig. 3). Specifically, Ti_3O_6 clusters are seen to cover the entire length of the step edges [Fig. 3(a)], with most bound as individual clusters that are roughly equally spaced. Moreover, the STM images show that the Ti_3O_6 cluster preferentially binds at the top of the steps. By contrast, the step edges on the Ti_3O_5/Au(111) surface are not uniformly occupied, but show small groupings of clusters that span across several steps [see Fig. 3(b)]. The lower step and, to a lesser extent, the upper step show a larger fraction of cluster assemblies that extend outward from the step edge onto the terrace. The latter suggests that the steps can act as nucleation sites for forming larger fractal assemblies of the Ti_3O_5 clusters. The differences in step site occupation for the two clusters are attributed to differences in intercluster interactions, which affect the mobility of the clusters to sample different binding sites on the Au(111) surface. The fact that the Ti_3O_6 clusters are only found in small groupings of 2–4 clusters on the terraces, while all the nearby step sites are fully occupied, suggests that the Ti_3O_6 clusters can encounter another cluster without sticking and continue to diffuse across the surface to find step sites where the binding energy is apparently larger. By contrast, the formation of larger fractal-like assemblies of the Ti_3O_5 clusters requires intercluster interactions to be strong enough to promote sticking and growth, while inhibiting diffusion, even along the dendrimer perimeter.[58,60] At the coverages used here, the mobility of the Ti_3O_5 clusters is thus limited by encounters with other clusters and the more weakly binding step sites are largely unoccupied. Hence, the striking differences in cluster morphology and binding sites seen in Fig. 3 are most likely due to differences in cluster–cluster interactions that reflect the stoichiometry and Ti–O coordination in the Ti_3O_5 and Ti_3O_6 clusters.

Figure 4(a) shows an expanded region of the Ti_3O_6/Au(111) surface where the individual clusters making up the assemblies can be more easily seen. Line scans though the cluster "dimer" shown in Figure 4(b) are given in the right panels of Fig. 4. The clusters in the dimer-like structures have nearly identical heights of 6.5–6.8 Å with a measured separation of ~1.3 nm. The lateral sizes are likely to be overestimated by tip convolution. Other discernable clusters exhibit some variability in shape, size, and inter-cluster separation. These variations may be a result of different cluster bonding geometries or electronic perturbations induced by the proximity of other clusters.

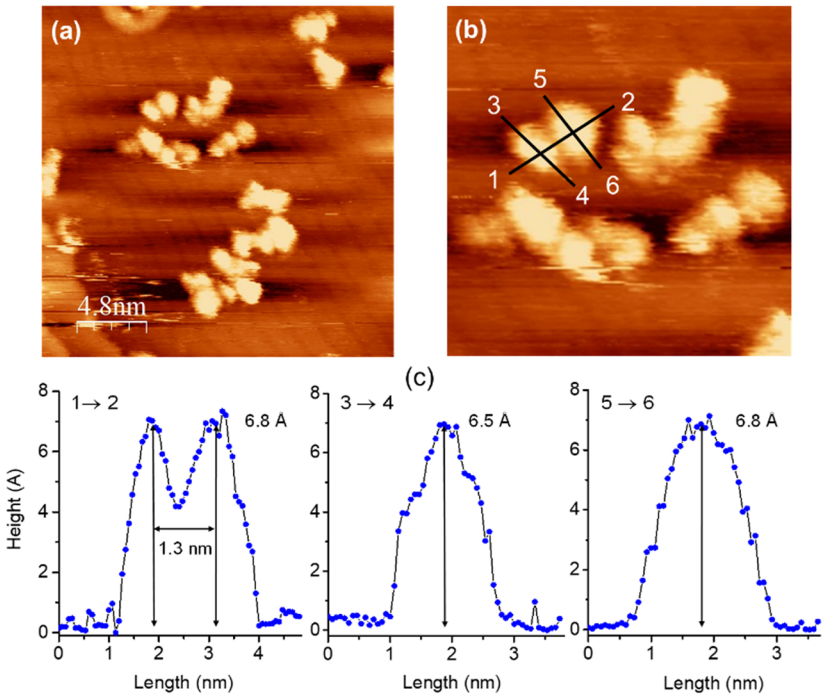

FIG. 4. (a) STM image showing small Ti_3O_6 cluster assemblies on Au(111) terraces at room temperature; image size 24 nm × 24 nm; (b) region of (a) expanded 2.5×; the numbered solid lines define the directions of the line profiles shown in (c); scan conditions: U = 2.1 V, I = 300 pA.

STM images of single clusters on terraces and steps (Fig. 5) show that there is a systematic height difference between the Ti_3O_6 and Ti_3O_5 clusters on both sites, with the Ti_3O_6 clusters about ~1 Å taller. This height difference is found for a large number of cluster height measurements shown in the histograms in Fig. S4 of the supplementary material. The single cluster images at steps [Figs. 5(c), 5(d), 5(f), and 5(g)] also suggest a height difference compared to the clusters on the terraces, and this may reflect differences in electron density or bonding configuration for clusters bound to at the steps.

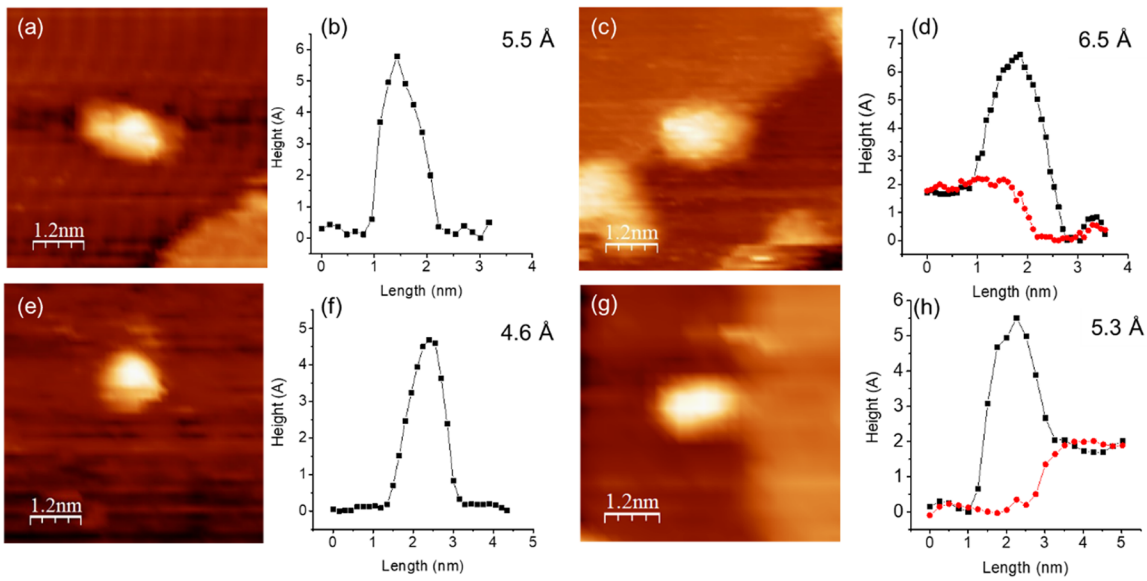

FIG. 5. STM images and corresponding line scans for single [(a) and (b)] Ti_3O_6 and [(e) and (f)] Ti_3O_5 clusters on Au(111) terraces and for single [(c) and (d)] Ti_3O_6 and [(g) and (h)] Ti_3O_5 clusters on Au(111) step edges. All image sizes: 6 nm × 6 nm. Scan conditions: (a) U = 2.0 V, I = 500 pA; (c) U = 1.7 V, I = 200 pA; (e) U = 1.9 V, I = 500 pA; (g) U = 2.0 V, I = 300 pA.

2. Surface morphology after annealing

To investigate the effects of surface heating on the assembly structure, STM images were obtained after annealing the surface at elevated temperatures in the range of 450 K–700 K. Specifically, the $Ti_3O_{5,6}$/Au(111) surfaces were heated (~1 K/s) and held at a target temperature for 3 min and then cooled and re-imaged at room temperature. Representative STM images following annealing at 450 K, 550 K, and 700 K are shown for both clusters in Fig. 6. The average numbers of clusters per assembly that are located on terraces as a function of annealing temperature are listed in Table I. The average number of clusters was determined from the weighted average of the measured assembly areas (Figs. S1 and S2) divided by the measured area of individual clusters such as those shown in Fig. 5 (Ti_3O_5, 1.7 nm^2; Ti_3O_6, 2.2 nm^2). This cluster counting is clearly approximate, but useful for contrasting the behavior of the two clusters and for temperature comparisons such as those in Table I.

For the Ti_3O_6/Au(111) surface, it can be seen from Figs. 6(a)–6(d) that the clusters are randomly distributed on the terraces. The average number of clusters in the assemblies shows a small increase at 450 K and decreases again at higher temperature, suggesting that the cluster groupings are constrained by a balance of cluster diffusion and inter-cluster interactions. Similarly, the cluster density along step sites does not show significant changes for temperatures up to 550 K [Figs. 6(b) and 6(c)]. After annealing to 700 K, the Au(111) surface shows considerable roughening with irregular step formation [Fig. 6(d)]. Clusters are still bound to the step edges, but as small groupings that extend out onto the terraces and with much larger lateral separation than at lower temperatures. Indeed, the strong binding of clusters to step sites could be responsible for the growth of irregular step edges due to the reduced mobility of Au atoms at these sites. Although the average numbers of Ti_3O_6 clusters per assembly on the terraces are similar at 550 K and 700 K (Table I), there are also a number of smaller particles (<10 Å), which may be due to fragmented TiO_x clusters.

TABLE I. The average number of clusters per assembly that are located on terraces as a function of annealing temperature.

	Annealing temperature			
Cluster	RT	450 K	550 K	700 K
Ti_3O_6	4 (3)[a]	5 (3)	3 (3)	4 (3)
Ti_3O_5	29 (30)	36 (54)	26 (26)	25 (24)

[a]The quantities in parentheses represent estimates of the widths of the size distributions at each temperature.

The sizes of the Ti_3O_5 cluster assemblies on the Au(111) terraces exhibit a similar trend with annealing temperature, i.e., a maximum at 450 K, but the decrease in size above 500 K is more pronounced [Figs. 6(e)–6(h) and Table I]. At 550 K, the steps also show a more uniform coverage of cluster assemblies, indicating diffusion of clusters from terrace to step sites above 450 K. The temperature behavior of the Ti_3O_5 fractal-like assemblies in Figs. 6(f) and 6(g) can be contrasted to that of similar dendritic islands formed by metal overlayers on metal supports, e.g., Au/Ru(0001), which transform to more regularly shaped, compact structures when heated to ~500 K.[60] At these temperatures, the metal atoms or clusters gain edge mobility, but unlike the metal atoms, the increased mobility of the oxide clusters is not sufficient to fuse the clusters into more regularly shaped, homogeneous TiO_x 2D islands. After annealing to 700 K, the Ti_3O_5/Au(111) surface also shows the formation of irregular step boundaries, but with much lower densities of cluster assemblies on the terraces and at the step edges. Small particles (<10 Å), which are likely to be TiO_x cluster fragments, are also observed after

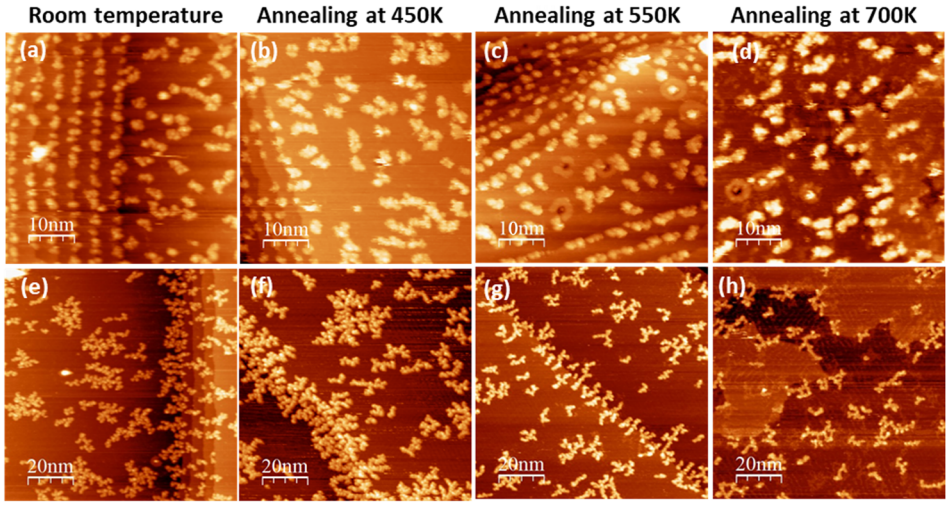

FIG. 6. STM images of [(a)–(d)] Ti_3O_6 clusters (0.26 ML) and [(e)–(h)] Ti_3O_5 clusters (0.24 ML) on Au(111); (a) and (e)] as-deposited surface at room temperature; [(b) and (f)] after annealing to 450 K; [(c) and (g)] after annealing to 550 K; [(d) and (h)] after annealing to 700 K. All images taken after sample were heated to annealing temperature for 3 min. and then cooled back to room temperature. Scan conditions: (a) U = 2.0 V, I = 300 pA, 50 nm × 50 nm; (b) U = 1.9 V, I = 400 pA, 50 nm × 50 nm; (c) U = 2.0 V, I = 700 pA, 50 nm × 50 nm; (d) U = 2.0 V, I = 400 pA, 50 nm × 50 nm; (e) U = 2.0 V, I = 200 pA, 100 nm × 100 nm; (f) U = 2.0 V, I = 300 pA, 100 nm × 100 nm; (g) U = 2.0 V, I = 700 pA, 100 nm × 100 nm; (h) U = 2.0 V, I = 400 pA, 100 nm × 100 nm.

the 700 K anneal and appear to form aligned linear arrays, some of which interconnect to form closed loops. The alignment of the fragments is similar to what might be expected for the dislocation lines of the Au(111) herringbone reconstruction, but the images are not sufficiently clear as to verify this possibility.

XPS spectra of the Ti 2p region taken after annealing to 450 K, 550 K, and 700 K are compared to the as-deposited spectra for the $Ti_3O_{5,6}$/Au(111) surfaces in Fig. S5. These spectra show that the Ti 2p peak intensities and binding energies are essentially the same for both cluster surfaces after annealing to temperatures ≤550 K. These observations suggest that the electronic environments of the Ti atoms in the clusters do not measurably change for moderate heating, which is consistent with STM images that show mostly changes in assembly size distributions over this temperature range (Fig. 6 and Table I). After heating to 700 K, the Ti 2p spectra for both cluster surfaces show an overall intensity loss of ~12% and small increases of ~5% in the Ti^{3+} contributions. In addition, the 700 K spectrum for the Ti_3O_6/Au(111) surface exhibits a shift of about +0.2 eV to higher binding energy. The decrease in the Ti signal and increased Ti^{3+} contributions after 700 K annealing may be the result of some cluster decomposition [Figs. 6(e) and 6(h)], with the resulting fragments experiencing greater Ti–Au interaction and perhaps some Ti atoms going subsurface.

C. Comparisons with DFT calculations

Figure 7 shows the calculated (DFT+U) lowest energy structures for the Ti_3O_6 and Ti_3O_5 clusters on the Au(111) surface. These structures were obtained by optimizing the gas-phase cluster[29,52–54] on the Au(111) surface starting from different initial orientations of the cluster relative to the surface. From the top down views in Fig. 7, it can be seen that two of the Ti atoms in the Ti_3O_6 cluster are coordinated to four oxygen atoms with no direct bonds to the Au, while the third Ti atom is bound to three oxygen atoms and the Au surface. The situation is reversed in the Ti_3O_5 cluster, which has only one Ti atom that is coordinated to four oxygen atoms, while the other two are bonded to three oxygen atoms and the Au surface. These two types of Ti atoms will be denoted by their oxygen coordination as Ti_{3c} and Ti_{4c}.

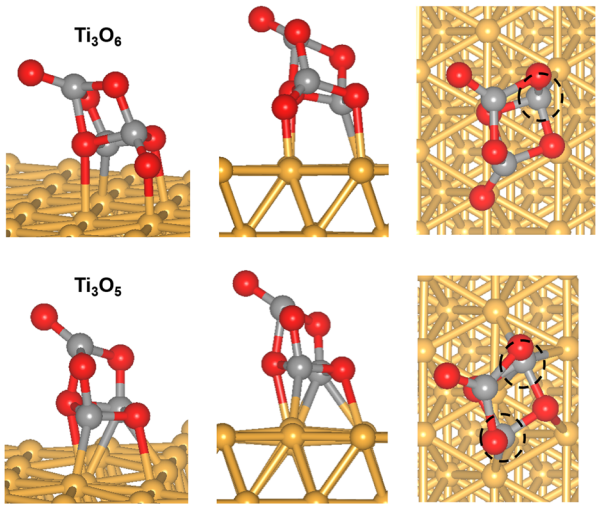

FIG. 7. DFT+U calculated minimum energy structures for the Ti_3O_6 and Ti_3O_5 clusters on Au(111). The dotted circles denote the positions of three-coordinate Ti_{3c} sites. Atom colors: red = O; gray = Ti; gold = Au.

The presence of two Ti_{3c} sites in the Ti_3O_5 cluster vs one in Ti_3O_6 can explain the larger Ti^{3+} contributions to the Ti 2p spectrum for the former (Fig. 2); however, the experimental Ti^{3+}/Ti^{4+} ratios for Ti_3O_5 (30%) and Ti_3O_6 (19%) are roughly half that expected from the DFT calculations, i.e., 2/3 and 1/3, respectively. The DFT calculations also predict that the binding energy [Eq. (1)] for the Ti_3O_5 cluster (−2.44 eV) is higher than that for the Ti_3O_6 cluster (−1.87 eV). This result is consistent with the Bader charge analyses (see the supplementary material, Fig. S6), which predict that the two Ti_{3c}–Au bonds at the Ti_3O_5-interface involve about −1*e* transfer from the cluster to the Au surface, whereas electron transfer is negligible for the Ti_3O_6/Au(111) surface. The larger charge transfer at the Ti_3O_5–Au(111) interface is indicative of stronger cluster-support electronic interactions and is consistent with a higher binding energy.

At first look, the higher binding energy of the Ti_3O_5 cluster compared to the Ti_3O_6 cluster seems at odds with the latter forming larger cluster assemblies, which presumably require higher cluster mobility. An alternative explanation is that both clusters have high mobility, but there is a larger driving force for the Ti_3O_5 clusters to couple after a diffusional encounter. Based on the calculated structures in Fig. 7, it seems reasonable that the formation of cluster assemblies is mediated by interactions between undercoordinated Ti_{3c} sites of one cluster with terminal oxygen atoms of another nearby cluster. With two of these Ti_{3c} edge sites, the Ti_3O_5 cluster should have a higher propensity to form assemblies of interacting clusters as compared to the Ti_3O_6 cluster, which has only one Ti_{3c} site. In the limit of small energy barriers, these interactions could even lead to the formation of Ti–O intercluster bonds to make dimers or even larger n-mers. In the case of the Ti_3O_6 cluster, the Ti_{3c} site may also be involved in bonding to undercoordinated Au atoms at step edges, which, according to the STM images, are the preferred binding sites on the Au(111) surface (Figs. 3 and 6). Binding at the step edge could effectively block the Ti_{3c} sites and prevent these clusters from forming dimers or other weakly bound cluster assemblies. Indeed, the STM images show that the Ti_3O_6 clusters bind almost exclusively as single particles at the step edges and do not act as nucleation points for the growth of larger assemblies. Hence, it is not surprising that only the Ti_3O_6 clusters on the terraces are observed to form cluster assemblies that involve only a few clusters (see Fig. 3 and Table I).

The formation of networks of covalently linked clusters is generally inconsistent with the STM images presented in Figs. 3–5, which clearly show distinguishable particles in the cluster assemblies. Furthermore, the observation that the assemblies change average size (Table I) after heating to moderate temperatures (450 K and 550 K; Fig. 6) would also be surprising for clusters held together by strong Ti–O bonds. More likely, the differences in the assembly sizes for the Ti_3O_5 and Ti_3O_6 clusters result from differences in intercluster electrostatic interactions that reflect the number of Ti_{3c} sites via the overall charge distributions of the clusters. Weaker electrostatic interactions are consistent with the results of thermal annealing and also suggest that the clusters can retain their unique chemical properties despite forming larger aggregates. The latter question is addressed in the reactivity studies described below.

D. Partial oxidation of 2-propanol on $Ti_3O_{5,6}$/Au(111) surfaces

As discussed above, the reduced Ti_3O_5 and stoichiometric Ti_3O_6 clusters supported on Au(111) are predicted to have different numbers of undercoordinated Ti_{3c} sites. The latter could act as active sites for redox reactions, analogous to oxygen vacancies on bulk TiO_2 surfaces. Intercluster interactions, which lead to the formation of cluster assemblies, could also block or reduce the number of these Ti_{3c} sites and thereby decrease the inherent activity of the isolated clusters. To test whether the reduced and stoichiometric clusters exhibit distinct reactivity, we examined the partial oxidation reactions of 2-propanol on the $Ti_3O_{5,6}$/Au(111) surfaces using temperature programmed desorption (TPD). The primary decomposition reactions on metal oxide surfaces are dehydration to propene and dehydrogenation to acetone, i.e.,

$$(CH_3)_2CHOH \rightarrow CH_3CHCH_2 + H_2O(\text{dehydration}), \quad (R1)$$

$$(CH_3)_2CHOH \rightarrow (CH_3)_2CO + H_2(\text{dehydrogenation}). \quad (R2)$$

On TiO_2 single crystals[61–65] and TiO_x supported on other oxides,[66] the decomposition of 2-propanol leads exclusively to the dehydration product, propene, while on TiO_2 powders, a small fraction of acetone is produced via reaction (R2).[67,68] At temperatures >450 K, the propene and acetone products result from the decomposition of propoxide intermediates formed by the deprotonation of 2-propanol at undercoordinated Ti^{3+} cation sites associated with oxygen vacancies. To form propene, the propoxide undergoes β-hydrogen transfer to a nearby surface oxygen atom to form a hydroxyl group, followed by C–O bond breaking [reaction (R2)].[61,63,67] In this way, propene formation heals the vacancy, which can be regenerated by water desorption via the recombination (disproportionation) of two hydroxyls. Vacancy sites generated by water desorption at higher temperature (>500 K) can also be occupied by propoxide species initially adsorbed at 5-coordinate Ti^{4+} sites and undergo dehydration to propene.[64] The acetone product results from α-hydride elimination from propoxide species followed by desorption of acetone, which leaves the vacancy site behind and the hydrogen atom stays on the surface as a hydroxyl or metal hydride [reaction (R2)]. The latter can also recombine and desorb as H_2 or as water, the latter resulting in further reduction of the surface.[61,62,67,68] The small yield of acetone from secondary alcohols like 2-propanol on titania single crystal surfaces is likely a result of steric hindrance of the α-hydride elimination reaction since the corresponding aldehydes are formed from primary alcohols such as ethanol and 1-propanol, which do not have bulky methyl side groups.[61,64]

The TPD spectra for a number of mass fragments from 2-propanol reactions on clean Au(111) and $Ti_3O_{5,6}$/Au(111) surfaces are shown in Fig. 8. The surfaces were prepared by exposure to 2-propanol at 120 K using a directed doser to minimize signal contributions from the background and desorption from the supporting sample holder. The 2-propanol coverage corresponds to multilayer formation as evidenced by the low temperature peaks on the bare Au(111) and $Ti_3O_{5,6}$/Au(111) surfaces near 190 K.[69] This dose was used to ensure saturation of cluster binding sites and is expected to have little effect on the high temperature (>350 K) product peak positions or intensities, which are the main interest of this study. Since the clusters do not cover the entire surface of the Au(111) support, the bare regions of the Au support contribute to the measured TPD spectra for the $Ti_3O_{5,6}$/Au(111) surfaces, although they are unreactive toward 2-isopropanol. Based on published mass fragmentation patterns at 70 eV electron ionization energies,[70] the ion fragments at masses 59 and 45 are mostly from 2-propanol, masses 58 and 43 from acetone, and mass 42 from propene. The ion signals for 2-propanol include reversible desorption of the intact molecule and the recombination of propoxy and H-atoms from surface hydroxyls to form 2-propanol that desorbs. The fragmentation of 2-propanol in the mass spectrometer ionizer also produces ion fragments at masses 43 and 42, which causes the TPD spectra for masses 59, 45, 43, and 42 to look similar at temperatures below 300 K. At temperatures above 350 K, the TPD spectra for masses 42 and 43 are dominated by the propene dehydration and acetone dehydrogenation products, respectively. Although small, the mass 58 signal corresponds to the parent ion for acetone and has essentially no contributions from 2-propanol; it is used as a consistency check for the acetone yield calculations based on the TPD data for the stronger signal at mass 43. Additional details concerning

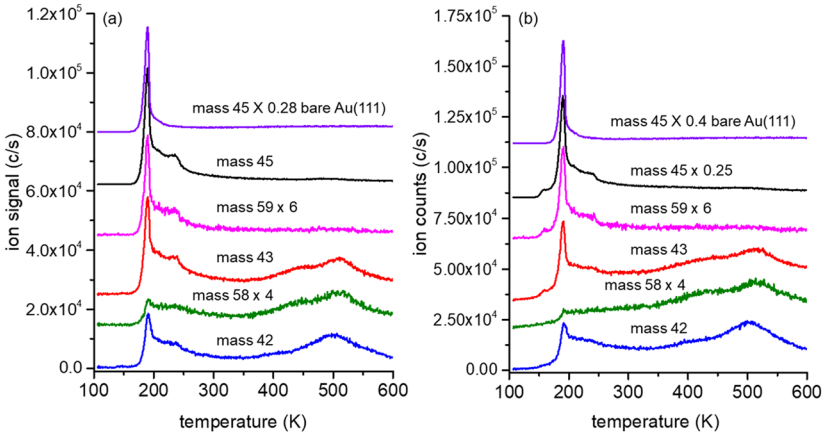

FIG. 8. TPD spectra for various product ions resulting from reactions of 2-propanol on (a) Ti_3O_6/Au(111) and (b) Ti_3O_5/Au(111) surfaces. Mass 45 is a primary fragment of 2-propanol, mass 59 is the parent mass of 2-propanol, mass 43 is a primary fragment of the acetone parent, mass 58 is the parent mass of acetone, and mass 42 is a primary fragment of propene.

the analysis of the TPD ion signals are given in the supplementary material.

Below 300 K, the TPD spectra for the various masses from the cluster surfaces exhibit a broad intensity shoulder in the range of 200–250 K with a distinct maximum at ~240 K. These features are more clearly seen in Fig. 9, where the Au(111) contribution to the mass 45 signal has been subtracted. By comparison, the mass 45 spectrum (2-propanol) from clean Au(111) shows a smaller and featureless shoulder over the same temperature range, which previous studies have shown to be associated with monolayer adsorption on the Au surface.[69] On slightly reduced TiO_2(110)[63,64] and TiO_2 nanocrystallites (5–10 nm) grown on the Au(111) surface,[39] 2-propanol desorption exhibits a peak around 320 K for coverages near a monolayer with a tail that extends out to 450–500 K (see Fig. 9). In both cases, the 2-propanol desorbed near 320 K is thought to originate from propoxide species (or intact 2-propanol) binding at Ti^{4+} sites. From the data in Fig. 8, the peak of 2-propanol desorption occurs at lower temperature (~240 K) with a tail that extends to a higher temperature. Based on the work cited above, we tentatively assign the low temperature (200–250 K) desorption of 2-propanol to adsorption at Ti^{4+} sites.[63] The 2-propanol molecules could be a result of reversible desorption of intact 2-propanol molecules or recombination of propoxide and hydrogen from a nearby bridged hydroxyl group. The lower temperature of the 2-propanol peak on the cluster/Au(111) surfaces may reflect the relatively high coverage used in this work as the bulky methyl groups of the 2-propanol (propoxide) molecules may introduce steric repulsions if more than one molecule binds to the small clusters.

The relative yields of the 2-propanol, propene, and acetone desorption products are shown in Fig. 9 for both clusters. Here, the TPD spectra for the fragments at masses 42, 43, and 58 have been corrected for contributions from the Au(111) surface and from fragment ions from 2-propanol and then converted to total acetone and propene yields using published electron impact fragmentation ratios for the parent 2-proponal, acetone, and propene molecules.[70] In this way, the corrected TPD spectrum for mass 42 represents the temperature dependent yield of the propene product. Likewise, the corrected TPD spectra for masses 43 and 58 give the yield of acetone products, and the two spectra overlap with each other as required. To make comparisons of the product distributions more quantitative, the areas of propene and acetone TPD spectra were summed from 350 K to 600 K and used as measures of the total product yields. This temperature range captures the high temperature signals for acetone and propene (summing over the entire temperature range, 200–600 K, only changes the relative yields by ~10%). The fractions of propene and acetone formed by each cluster and the relative propene and acetone yields are given in Table II.

The two most important observations from Fig. 9 and Table II are as follows: (1) both clusters promote the dehydration (propene product) *and* the dehydrogenation (acetone product) of 2-propanol and (2) the reduced Ti_3O_5 cluster is roughly 2× more reactive than the stoichiometric Ti_3O_6 cluster. We attribute the higher activity of the Ti_3O_5 cluster with the higher number of undercoordinated Ti_{3c} sites (2) compared to the Ti_3O_6 cluster (1). This conclusion is consistent with previous studies on TiO_2(110) surfaces that found that the yield of propene at high temperature (>500 K) increases with surface vacancy concentrations.[62–65] The difference in activity also demonstrates that the Ti_3O_5 and Ti_3O_6 clusters remain chemically distinct despite intercluster interactions that lead to the formation of cluster assemblies (Fig. 3). We also note that the level of reduction of the clusters as measured by the percentage of Ti^{3+} signals in the Ti2p spectra did not change appreciably after TPD reactions of 2-propanol (less than 1%; spectra not shown). This indicates that the hydroxyl group that is added to the cluster via the dehydration reaction to propene is subsequently removed by water desorption. Although we were not able to measure desorption of H_2O (mass 18) from the surface reaction due to interference with background water in the vacuum chamber, water desorption associated with propene formation has been observed from ~300 K to 600 K on single crystal TiO_2(110) surfaces and titania powders.[62,63,67]

The observation of acetone in significant quantities (~30% of the total product yield; Table II) appears to be unique to systems that involve combinations of both TiO_2 and Au. Specifically, small Au

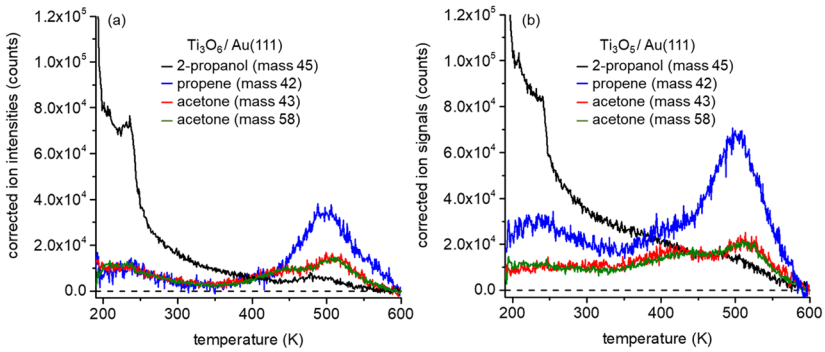

FIG. 9. Relative product yields for 2-propanol reactions on (a) Ti_3O_6 and (b) Ti_3O_5 clusters supported on Au(111) as determined from the TPD measurements shown in Fig. 1. The 2-propanol and propene products were obtained from the ion fragments with mass 45 and mass 42, respectively, while the acetone product was independently determined from the mass 43 and mass 58 fragments. The conversion of ion intensities to product yields was performed by removing contributions from the Au(111) bare surface at each mass and then correcting for contributions from the parent and other fragment ions at the same mass on the $Ti_3O_{5,6}$/Au(111) surface. See text and supplementary material for more details.

TABLE II. Relative product yields for acetone and propene from reactions of 2-propanol on Ti_3O_6 and Ti_3O_5 clusters on Au(111) as determined from the TPD results in the temperature range of 350–600 K (see Fig. 9).

	Acetone/total[a]	Propene/total[a]	Propene ratio	Acetone ratio
Ti_3O_6	0.33 ± 0.03	0.67 ± 0.03	...	...
Ti_3O_5	0.28 ± 0.03	0.72 ± 0.03	...	...
Ti_3O_5/Ti_3O_6	...		2.32 ± 0.02	1.93 ± 0.02

[a]Total = sum of propene and acetone product yields.

nanoparticles (NPs) deposited on TiO_2 powders[66–68] or Ti nanocrystallites (5–20 nm)[39] and our small $Ti_3O_{5,6}$ clusters deposited onto Au(111) all produce acetone in significant quantities, with the titania supported Au NP systems having even higher selectivity for acetone than propene. Partial oxidation of ethanol to ethylene and acetaldehyde was also observed in TPD experiments from surfaces of TiO_x nanoparticles (~10 nm diam; 0.6 ML) supported on Au(111).[38] In all these previous experiments, the dehydrogenation activity to form the aldehyde was attributed to active sites at the Au–TiO_2 interface.[66–68] The proposed mechanism at the Au–TiO_2 interface involves deprotonation and propoxide binding on TiO_x, with β-hydrogen transfer promoted by Au-hydride formation at the interface, thus leading to the acetone product.[66,68,71] Hence, the sizeable yield of acetone relative to propene on the $Ti_3O_{5,6}$/Au(111) surfaces likely reflects the fact that all of the Ti active sites in these small clusters lie at the periphery and are accessible at the Au interface. By comparison, the comparably small W_3O_9 cluster, unsupported and supported on TiO_2(110), only promotes the dehydration of 2-propanol to propene.[72,73] Since the dehydrogenation reaction must take place on the W_3O_9 cluster itself, the β-hydrogen transfer required for acetone formation is likely to be sterically hindered by the bulky methyl groups of 2-propanol. This is supported by the fact that reactions of the primary alcohols on the W_3O_9 cluster result in small yields of the corresponding aldehyde.[73] For the Au supported clusters studied here, the $Ti_3O_{5,6}$–Au interface offers more possible configurations for β-hydrogen transfer to nearby Au atoms, consistent with the higher yields of the dehydrogenation product acetone.

In addition to the data presented for the first TPD cycle, we also performed two more consecutive TPD runs to see if the surface remains active after reaction with 2-propanol and heating to 600 K. As shown in Fig. S7, the yields of propene and acetone products for both the Ti_3O_5/Au(111) and Ti_3O_6/Au(111) surfaces decrease significantly in the 2nd TPD run, while the 2nd and 3rd TPD runs have very similar yields. These data suggest that the surface is irreversibly changed after the first TPD heating cycle. This loss of activity for TPD runs up to 600 K may be a combination of both thermal and reaction induced deactivation of the clusters. Although the decrease in activity after the first TPD run indicates the loss of active sites for reaction, the Ti_3O_5/Au(111) surface remains more active (~1.4×) for propene formation than the Ti_3O_5/Au(111) surface for the 2nd and 3rd runs (acetone yields are comparable).

IV. SUMMARY

The morphology and clustering of mass-selected Ti_3O_6 and "reduced" Ti_3O_5 clusters deposited on Au(111) were found to be strikingly different despite the fact that the clusters differ by only one oxygen atom. STM images show that the Ti_3O_6 cluster decorates step edges and forms small cluster assemblies of 2–4 clusters on terraces. By contrast, the "reduced" Ti_3O_5 cluster forms much larger fractal-like assemblies involving tens of clusters. In both cases, individual clusters are distinguishable within the cluster assemblies, suggesting that they are in contact but not chemically fused. Calculations of the optimized cluster structures on the Au(111) surface show that the Ti_3O_5 cluster has two 3-fold coordinated Ti sites (Ti_{3c}) vs only one for the Ti_3O_6 cluster, which is consistent with a larger contribution of Ti^{3+} in the Ti 2p XPS spectra of the Ti_3O_5/Au(111) surface. Annealing experiments show that the sizes of the assemblies increased for both clusters for temperatures up to 450 K, while at higher temperatures (500–600 K), the assemblies decreased in size along with the appearance of some smaller objects that could be cluster fragments. At 700 K, the Au surface becomes disrupted with irregular steps, which may be due to reduced mobility of Au atoms due to strong interactions with the clusters. Overall, the annealing experiments show that the clusters retain their identity for temperatures up to 600 K without sintering into larger 2D or 3D TiO_x islands. Differences in reactivity for 2-propanol dehydration and dehydrogenation observed in TPD measurements show that the Ti_3O_6 and Ti_3O_5 clusters retain their chemical identity despite forming cluster assemblies and/or bonding at step edges. Specifically, the reduced Ti_3O_5 cluster exhibits roughly twice the activity of the stoichiometric Ti_3O_6 cluster, which is attributed to the presence of two Ti_{3c} sites in Ti_3O_5 vs only one for Ti_3O_6. Both clusters also exhibit substantial activity for 2-propanol dehydrogenation to acetone, which appears to be unique to TiO_x–Au interfaces. Overall, the results of this work demonstrate how it is possible to modify the secondary morphology and reactivity of small metal oxide clusters through control of stoichiometry and cation coordination.

SUPPLEMENTARY MATERIAL

See the supplementary material for measured distributions of the cluster assembly areas, fractal dimension calculation, calculated cluster structures with Bader charges, XPS spectra following surface annealing, and a detailed description of how the 2-propanol TPD spectra were converted to relative product yields.

ACKNOWLEDGMENTS

This work was performed at Brookhaven National Laboratory and used resources of the Center for Functional Nanomaterials, a U.S. DOE Office of Science User Facility. K.R.G., J.W., Y.M., and M.G.W. were supported by the U.S. Department of Energy (DOE), Office of Science, Office of Basic Energy Sciences, Chemical Sciences, Geosciences, and Biosciences (CSGB) Division, and the Catalysis Science Program under DOE Contract No. DE-SC0012704. D.J.S. was supported by Integrated Mesoscale Architectures for Sustainable Catalysis (IMASC), an Energy Frontier Research Center funded by the U.S. Department of Energy, Office of Science, Basic Energy Sciences under Award No. DE-SC0012573.

REFERENCES

[1] Q. Fu and T. Wagner, Surf. Sci. Rep. **62**, 431–498 (2007).
[2] A. Bruix, J. A. Rodriguez, P. J. Ramirez, S. D. Senanayake, J. Evans, J. B. Park, D. Stacchiola, P. Liu, J. Hrbek, and F. Illas, J. Am. Chem. Soc. **134**, 8968–8974 (2012).
[3] G. Pacchioni, Phys. Chem. Chem. Phys. **15**, 1737–1757 (2013).
[4] C. T. Campbell, Nat. Chem. **4**, 597 (2012).
[5] J. A. Rodriguez, P. Liu, X. Wang, W. Wen, J. Hanson, J. Hrbek, M. Pérez, and J. Evans, Catal. Today **143**, 45–50 (2009).
[6] J. A. Rodriguez, J. Graciani, J. Evans, J. B. Park, F. Yang, D. Stacchiola, S. D. Senanayake, S. Ma, M. Pérez, P. Liu, J. F. Sanz, and J. Hrbek, Angew. Chem., Int. Ed. **48**, 8047–8050 (2009).
[7] J. A. Rodríguez, J. Evans, J. Graciani, J.-B. Park, P. Liu, J. Hrbek, and J. F. Sanz, J. Phys. Chem. C **113**, 7364–7370 (2009).
[8] J. A. Rodriguez, S. Ma, P. Liu, J. Hrbek, J. Evans, and M. Pérez, Science **318**, 1757–1760 (2007).
[9] F. Yang, J. Graciani, J. Evans, P. Liu, J. Hrbek, J. F. Sanz, and J. A. Rodriguez, J. Am. Chem. Soc. **133**, 3444–3451 (2011).
[10] R. M. Palomino, R. A. Gutierrez, Z. Y. Liu, S. Tenney, D. C. Grinter, E. Crumlin, I. Waluyo, P. J. Ramirez, J. A. Rodriguez, and S. D. Senanayake, ACS Sustainable Chem. Eng. **5**, 10783–10791 (2017).
[11] Z. Y. Duan and G. Henkelman, ACS Catal. **5**, 1589–1595 (2015).
[12] H. Koga, K. Tada, and M. Okumura, J. Phys. Chem. C **119**, 25907–25916 (2015).
[13] I. X. Green, W. Tang, M. Neurock, and J. T. Yates, Acct. Chem. Res. **47**, 805–815 (2014).
[14] L. B. Vilhelmsen and B. Hammer, ACS Catal. **4**, 1626–1631 (2014).
[15] K. Mitsuhara, M. Tagami, T. Matsuda, A. Visikovskiy, M. Takizawa, and Y. Kido, J. Chem. Phys. **136**, 124303 (2012).
[16] I. X. Green, W. J. Tang, M. Neurock, and J. T. Yates, Science **333**, 736–739 (2011).
[17] L. M. Molina and B. Hammer, Appl. Catal. A: Gen. **291**, 21–31 (2005).
[18] H. L. Tang, Y. Su, B. S. Zhang, A. F. Lee, M. A. Isaacs, K. Wilson, L. Li, Y. G. Ren, J. H. Huang, M. Haruta, B. T. Qiao, X. Liu, C. Z. Jin, D. S. Su, J. H. Wang, and T. Zhang, Sci. Adv. **3**, e1700231 (2017).
[19] S. J. Tauster, Acct. Chem. Res. **20**, 389–394 (1987).
[20] G. L. Haller and D. E. Resasco, in *Advances in Catalysis*, edited by D. D. Eley, H. Pines, and P. B. Weisz (Academic Press, 1989), Vol. 36, pp. 173–235.
[21] E. J. Braunschweig, A. D. Logan, A. K. Datye, and D. J. Smith, J. Catal. **118**, 227–237 (1989).
[22] G. N. Vayssilov, Y. Lykhach, A. Migani, T. Staudt, G. P. Petrova, N. Tsud, T. Skála, A. Bruix, F. Illas, K. C. Prince, V. Matolíin, K. M. Neyman, and J. Libuda, Nat. Matter **10**, 310 (2011).
[23] C. Linsmeier and E. Taglauer, Appl. Catal. A: Gen. **391**, 175–186 (2011).
[24] T. Lunkenbein, J. Schumann, M. Behrens, R. Schlögl, and M. G. Willinger, Angew. Chem., Int. Ed. **54**, 4544–4548 (2015).
[25] J. Schoiswohl, S. Surnev, and F. P. Netzer, Top. Catal. **36**, 91–105 (2005).
[26] J. Schoiswohl, M. Sock, Q. Chen, G. Thornton, G. Kresse, M. G. Ramsey, S. Surnev, and F. P. Netzer, Top. Catal. **46**, 137–149 (2007).
[27] J. A. Rodríguez and J. Hrbek, Surf. Sci. **604**, 241–244 (2010).
[28] J. A. Rodriguez, P. Liu, J. Graciani, S. D. Senanayake, D. C. Grinter, D. Stacchiola, J. Hrbek, and J. Fernández-Sanz, J. Phys. Chem. Lett. **7**, 2627–2639 (2016).
[29] Y. X. Yang, J. Zhou, M. Nakayama, L. Z. Nie, P. Liu, and M. G. White, J. Phys. Chem. C **118**, 13697–13706 (2014).
[30] M. Nakayama, M. Xue, W. An, P. Liu, and M. G. White, J. Phys. Chem. C **119**, 14756–14768 (2015).
[31] M. Xue, M. Nakayama, P. Liu, and M. G. White, J. Phys. Chem. C **121**, 22234–22247 (2017).
[32] J. Zhou and D. A. Chen, Surf. Sci. **527**, 183–197 (2003).
[33] F. Coloma, F. Marquez, C. H. Rochester, and J. A. Anderson, Phys. Chem. Chem. Phys. **2**, 5320–5327 (2000).
[34] J. Zhou, Y. C. Kang, and D. A. Chen, Surf. Sci. **537**, L429–L434 (2003).
[35] S. C. Parker and C. T. Campbell, Top. Catal. **44**, 3–13 (2007).
[36] L. Zhang, R. Persaud, and T. E. Madey, Phys. Rev. B **56**, 10549–10557 (1997).
[37] X. Lai, T. P. St Clair, M. Valden, and D. W. Goodman, Prog. Surf. Sci. **59**, 25–52 (1998).
[38] D. T. Boyle, J. A. Wilke, R. M. Palomino, V. H. Lam, D. A. Schlosser, W. J. Andahazy, C. Z. Stopak, D. J. Stacchiola, J. A. Rodriguez, and A. E. Baber, J. Phys. Chem. C **121**, 7794–7802 (2017).
[39] D. V. Potapenko, Z. Li, Y. Lou, Y. Guo, and R. M. Osgood, J. Catal. **297**, 281–288 (2013).
[40] Z. Song, J. Hrbek, and R. Osgood, Nano Lett. **5**, 1327–1332 (2005).
[41] D. V. Potapenko and R. M. Osgood, Nano Lett. **9**, 2378–2383 (2009).
[42] I. Horcas, R. Fernández, J. M. Gómez-Rodríguez, J. Colchero, J. Gómez-Herrero, and A. M. Baro, Rev. Sci. Instrum. **78**, 013705 (2007).
[43] G. Kresse and J. Furthmüller, Comput. Mater. Sci. **6**, 15–50 (1996).
[44] G. Kresse and J. Furthmüller, Phys. Rev. B **54**, 11169–11186 (1996).
[45] G. Kresse and J. Hafner, Phys. Rev. B **47**, 558–561 (1993).
[46] J. P. Perdew, J. A. Chevary, S. H. Vosko, K. A. Jackson, M. R. Pederson, D. J. Singh, and C. Fiolhais, Phys. Rev. B **46**, 6671 (1992).
[47] G. Kresse and D. Joubert, Phys. Rev. B **59**, 1758–1775 (1999).
[48] S. L. Dudarev, G. A. Botton, S. Y. Savrasov, C. J. Humphreys, and A. P. Sutton, Phys. Rev. B **57**, 1505–1509 (1998).
[49] Z. P. Hu and H. Metiu, J. Phys. Chem. C **115**, 5841–5845 (2011).
[50] M. Setvin, C. Franchini, X. Hao, M. Schmid, A. Janotti, M. Kaltak, C. G. Van de Walle, G. Kresse, and U. Diebold, Phys. Rev. Lett. **113**, 086402 (2014).
[51] H. J. Monkhorst and J. D. Pack, Phys. Rev. B **13**, 5188 (1976).
[52] M. L. Weichman, X. Song, M. R. Fagiani, S. Debnath, S. Gewinner, W. Schöllkopf, D. M. Neumark, and K. R. Asmis, J. Chem. Phys. **144**, 124308 (2016).
[53] S. Li and D. A. Dixon, J. Phys. Chem. A **112**, 6646–6666 (2008).
[54] Z.-w. Qu and G.-J. Kroes, J. Phys. Chem. B **110**, 8998–9007 (2006).
[55] J. Biener, E. Farfan-Arribas, M. Biener, C. M. Friend, and R. J. Madix, J. Chem. Phys. **123**, 094705 (2005).
[56] U. Diebold, Surf. Sci. Rep. **48**, 53–229 (2003).
[57] P. Meakin, Phys. Rev. A **27**, 1495–1507 (1983).
[58] H. Brune, Surf. Sci. Rep. **31**, 121–229 (1998).
[59] B. Florio, P. Fawell, and M. Small, Powder Technol. **343**, 551–559 (2019).
[60] R. Q. Hwang, C. Günther, J. Schröder, S. Günther, E. Kopatzki, and R. J. Behm, J. Vac. Sci. Technol. A **10**, 1970–1980 (1992).
[61] K. S. Kim and M. A. Barteau, J. Mol. Catal. **63**, 103–117 (1990).
[62] E. Farfan-Arribas and R. J. Madix, J. Phys. Chem. B **106**, 10680–10692 (2002).
[63] O. Bondarchuk, Y. K. Kim, J. M. White, J. Kim, B. D. Kay, and Z. Dohnalek, J. Phys. Chem. C **111**, 11059–11067 (2007).
[64] Y. K. Kim, B. D. Kay, J. M. White, and Z. Dohnálek, Surf. Sci. **602**, 511–516 (2008).
[65] Y. K. Kim, B. D. Kay, J. M. White, and Z. Dohnalek, J. Phys. Chem. C **111**, 18236–18242 (2007).
[66] Y. Y. Wu and H. H. Kung, Appl. Catal. A **548**, 150–163 (2017).
[67] K. S. Kim, M. A. Barteau, and W. E. Farneth, Langmuir **4**, 533–543 (1988).
[68] M. C. Holz, K. Kähler, K. Tölle, A. C. van Veen, and M. Muhler, Phys. Status Solidi B **250**, 1094–1106 (2013).
[69] J. Gong, D. W. Flaherty, T. Yan, and C. B. Mullins, ChemPhysChem **9**, 2461–2466 (2008).
[70] W. E. Wallace, in *NIST Chemistry WebBook, NIST Standard Reference Database Number 69*, edited by P. J. Linstrom and W. G. Mallard (National Institute of Standards and Technology, Gaithersburg, MD, 2019).
[71] M. A. Nadeem, I. Majeed, G. I. N. Waterhouse, and H. Idriss, Catal., Struct. React. **1**, 61–70 (2015).
[72] Y. K. Kim, R. Rousseau, B. D. Kay, J. M. White, and Z. Dohnálek, J. Am. Chem. Soc. **130**, 5059–5061 (2008).
[73] Y. K. Kim, Z. Dohnálek, B. D. Kay, and R. Rousseau, J. Phys. Chem. C **113**, 9721–9730 (2009).